**Chapter 14**
**Nanoscale electromagnetic measurements for life science applications**

## 14.1 High-resolution optical microscopy of nanoscale biological systems

### *14.1.1 Far-field techniques*

The number of microscopic imaging applications related to biological systems is large and continues to grow. Fig. 14.1 shows the dimensions of selected, biological systems. Depending on the length scale of the system, a variety of different microscopy techniques are available. For comparison, Fig. 14.1 also illustrates comparable solid state, electronic systems at various length scales. In this chapter, we will describe methods for imaging and characterization of biological materials at sub-micrometer length scales. The focus will be on electrical scanning probe imaging methods, but by way of introduction we will discuss selected optical methods first. Our review of optical methods is but a brief survey of a small subset of many available techniques.

Figure 14.1. **Length scales of biological and electronic systems.** A comparison of length scales of biological (left) and electronic (right) systems that can be accessed by near-field scanning microwave microscopy and other measurement techniques.

Historically, the most prominent techniques for biomaterial imaging have been optical techniques, especially those based on fluorescence imaging. The importance of optical techniques is due in large part to the fact that they allow imaging of living cells with minimal invasiveness. Although electron microscopy has better spatial resolution, optical microscopy still dominates biological research. The resolution of most optical microscopy has historically been diffraction-limited with resolution of approximately $0.6\lambda/NA$ where $\lambda$ is the wavelength of the light and *NA* is the numerical aperture of the microscope objective lens. Thus, at the diffraction limit of conventional fluorescent microscopies, resolution is on the order of 200 nm. This is practical in many cases, but if the molecules are separated by distances on the order of 200 nm to 350 nm, then it is not possible to tell them apart. As a result, it has been necessary to develop sub-diffraction-limit techniques in order to image nanoscale biological systems and distinguish the sub-systems within them.

One critical breakthrough in the imaging of life science systems was the development of tagging methods for proteins and other biological molecules by use of fluorescent probe molecules. Staining techniques for inducing contrast in optical images date back to the nineteenth century and played a central role in biological imaging of that period, such as the work of 1906 Nobel Prize winner Santiago Ramon y Cajal. More recently, the importance of tagging techniques has been acknowledged through two additional Nobel prizes. The first was in 2008 and was awarded to Shimomura, Tsien and Chalfie for the discovery and development of green, fluorescent protein. The second was in 2014 and was awarded to Betzing, Hell and Moerner for the development of super-resolution fluorescence microscopy. Indeed, the unique

photochemical properties of fluorescent molecules are the foundation for a number of sub-diffraction limit microscopies.

However, overcoming the diffraction limit is not merely about detecting tagged molecules, but also about distinguishing one molecule from another when the intermolecular separation is on the order of 100 nm or less. This is accomplished in large part by leveraging stimulated emission, as originally introduced by Hell [1]. Hell's approach was based on keeping a fraction of the molecules in the observation area in a dark state while the other, bright-state molecules in the observation area are detected. One strategy to keep some molecules in a dark, ground state is the use of stimulated emission. This idea led to stimulated emission depletion (STED) microscopy. The STED technique utilizes two lasers: one to excite the fluorophores and a second to deplete the excited-state through stimulated-emission before the fluorophores emit light through spontaneous fluorescence. In other words, one beam is used to illuminate the molecules and excite them into the bright state. The second light beam induces stimulated emission and returns the excited molecules into their ground (dark) state. By properly shaping the second beam into a ring in the focal plane, all the molecules but the ones at the center will be turned off. The effect of this second laser, referred to as a STED beam, is a drastic reduction in the size of the fluorescence spot. An image can subsequently be acquired by coordinated, overlapped scanning of the excitation and STED laser beams across the sample. At present there are several variants of this approach with 50 nm to 100 nm resolution.

Another approach to nanoscale microscopy, known as superlocalization, was pioneered by Moerner [2]. This approach built upon the work of Betzing, in which photo-switchable fluorescent proteins were employed as an active control mechanism for photoactivated localization microscopy (PALM). Experimentally, the technique relies on simultaneously suppressing background signals while maximizing emission from the molecules of interest. The fundamental analytical idea introduced by Moerner was overlaying the shape of the measured point-spread-function with a Gaussian (Airy) function. This innovation, which is at the heart of superlocalization, reduced the Abbe diffraction limit by a factor of $\sqrt{N}$, where *N* is the number of measurements. Put simply, two conceptually simple ideas are at the heart of this technique. The first is to use spectrally distinct tags in order to distinguish molecules in "multicolor" images. The second idea is to induce the molecules to emit sequentially such that they are not all emitting simultaneously. When combined with the superlocalization technique, these two ideas enable image reconstruction in which closely spaced molecules can be distinguished. The experimental technique has a number of different acronyms depending on the strategies for controlling emitting concentrations and sequential emission. Application of localization microscopies has improved spatial resolution to 20 to 50 nm scale [3].

### *14.1.2 Near-field techniques*

So far, we have limited our discussion to sub-diffraction-limit, optical techniques based on far-field observation. In this section, we turn to sub-diffraction-limit optical techniques that are based on near-field interactions. These near-field methods are topically closer to the preceding chapters and near-field

scanning microwave microscopy (NSMM), in particular. One example of a near-field optical technique is total internal reflection fluorescent microscopy (TIRF) [4]. TIRF utilizes evanescent waves to selectively illuminate and excite fluorophones in a specimen immediately adjacent to a glass-liquid interface. When the light is obliquely incident from the glass (substrate) side at an angle equal to or greater than the critical angle of refraction given by Snell's law, the light is totally reflected. During this process, a surface evanescent wave is generated at the interface. This effect is well-known and is called total internal reflection. Due to exponential decay of the amplitude of this wave from the surface the probed penetrated area of the specimen is given by

$$d = \frac{\lambda}{4\pi n_2}\left(\frac{sin^2\theta}{sin^2\theta_c} - 1\right)^{-1/2} \quad , \qquad (14.1)$$

where $\theta$ is the angle of incidence, $\theta_c = sin^{-1}(\frac{n_2}{n_1})$ is the critical angle of incidence, $\lambda$ is the free space wavelength of the incident light, $n_2$ is the refractive index of liquid medium, and $n_1$ is the refractive index of the substrate. For a typical system such as a glass-water interface, this represents a penetration depth of about 100 nm into the sample. The technique has been used to observe the fluorescence of a single molecule with the relative intensity of the molecular fluorescence depending on the distance of the molecule from the interface.

Near-field scanning optical microscopy (NSOM) is another, near-field optical technique the that was introduced after the discovery of scanning probe microscopes. It was originally developed by Betzing and Trautman [5]. As originally conceived, NSOM relies on optical radiation incident upon a subwavelength aperture. Thus, it shares its fundamental ideas with early NSMM. In one early realization of this technique, Ash and Nicholls used illumination of a small aperture that was a part of an open resonator to go beyond the diffraction limit [6]. Building upon this initial demonstration, Betzing and Trautman designed a successful NSOM by use of a glass capillary coated with aluminum. This first, near-field optical microscope surpassed the diffraction limit by a factor of two. Significant improvement was achieved when the capillary was replaced by a tapered optical fiber, leading to more efficient transmission of the light to the NSOM probe and improved coupling to the evanescent optical modes at the probe tip. At present, NSOM is used for a variety of applications, including optical data storage, super resolution photolithography and nano-spectroscopy.

## 14.2 Electrical characterization of biological systems

### *14.2.1 The measurement problem*

In addition to NSOM, there are a variety of other techniques to image biological objects by use of standard or modified scanning tunneling microscopes (STMs) and atomic force microscopes (AFMs). The properties of proteins, nucleic acids, membranes and cells have been studied by use of a broad range of AFM- and STM-based approaches [7]-[9]. The ultimate objective of this chapter is to describe the application of electrical, scanning-probe-based techniques, including NSMM, to life science metrology. However, before addressing the specific challenges related to NSMM of biological systems, we must answer several

broader questions about the electrical characterization of biological systems. How do we model the interaction of electromagnetic radiation with biological systems? What are the relevant material parameters and measurands of interest? What modifications must be made in order to extend the measurements to heterogeneous systems? Are any special considerations required to account for measuring in a liquid environment?

*14.2.2 Microwave antenna probes*

Interest in the application of microwave techniques to medical diagnostics is driven in part by the fact that microwave techniques are noninvasive. In fact, some tissues are transparent to microwaves. Potential applications include microwave heating therapy and cancer detection. The latter application is based on the fact that the conductivity of cancerous tissue is about a factor of five higher than that of healthy tissue [10]. Thus, the identification of malignant tissue is based on a temperature difference between malignant and healthy tissue. The temperature is measured indirectly through the spectral radiance of the electromagnetic radiation, which is given by

$$I(f,T) = \mu\varepsilon \frac{2hf^3}{e^{\frac{hf}{k_B T}} - 1} \quad , \tag{14.2}$$

where $\mu$ is the permeability of the medium, $\varepsilon$ is the permittivity of the medium, $h$ is Plank's constant, $f$ is the radiating frequency, $k_B$ is the Boltzmann constant, and $T$ is the temperature. Clearly, in order to realize such medical applications, one must understand the interaction of electromagnetic radiation with biological systems.

As we have previously noted in this book, accurate probe-sample models are required in order to extract material parameters from microwave probe measurements. The first such model that we will consider here is an *in vivo* microwave antenna probe. The operating principle of such a probe is based on the antenna modeling theorem, which can be expressed as

$$\frac{Z(\omega,\varepsilon^*)}{\sqrt{\mu_0/\varepsilon^*}} = \frac{Z(n\omega,\varepsilon_0)}{\sqrt{\mu_0/\varepsilon_0}} \tag{14.3}$$

where $Z$ is the terminal impedance of the antenna probe, $\varepsilon^*$ is the complex permittivity of the medium, $n = \sqrt{\varepsilon^*/\varepsilon_0}$ is the complex index of refraction of the medium, and $Z_0 = \sqrt{\mu_0/\varepsilon_0}$ is the impedance of free space. The left hand side of Equation (14.3) corresponds to the probe in the dielectric medium while the right hand side corresponds to the probe in free space. Equation (14.3) is derived under the assumption that the antenna is entirely contained within the medium and that the surrounding medium is infinite. This relationship can be applied to any type of microwave probe, provided that the terminal impedance of the probe is known. For a short monopole probe with length $\lambda/10$ or less, as is the case for the NSMM, the antenna impedance in free space is given by [11]

$$Z(\omega,\varepsilon_0) = A\omega^2 + \frac{1}{j\omega C} \quad , \tag{14.4}$$

where the constant *A* and the capacitance constant *C* are determined from the antenna's physical dimensions. When the antenna is in a lossy medium, it follows from Equations (14.3) and (14.4) that the impedance is

$$Z(\omega, \varepsilon^*) = R + jX \quad , \tag{14.5}$$

where

$$R = \frac{sin2\delta}{2\varepsilon'\omega C} + A\sqrt{\varepsilon'}\omega^2\sqrt{\frac{sec\delta+1}{2}} \quad , \tag{14.6a}$$

$$X = \frac{cos^2\delta}{\varepsilon'\omega C} + A\sqrt{\varepsilon'}\omega^2\sqrt{\frac{sec\delta-1}{2}} \quad . \tag{14.6b}$$

The dielectric constant has the form $\varepsilon^* = \varepsilon'\varepsilon_0(1 - jtan\delta)$. These equations can be solved iteratively, noting that $tan\delta = R/X$.

Equations (14.6) can be simplified for the case of an open-ended coaxial probe [11]-[13]. Generally, small-diameter coaxial lines are more appropriate for *in vivo* measurements. To model a coaxial probe, we begin by defining the reference capacitance of the open coaxial cable in air as $C_0$. If evanescent modes are taken into account, this capacitance has to be modified to have the form $C_0 + Af^2$, where *A* is once again a constant dependent on geometry. It is important to note that when the probe is inserted into a material, some of the evanescent modes may become propagating modes. The relation of the complex permittivity to the measured reflection coefficient from the antenna, $S_{11}$, comes from the standard definition of the reflection coefficient and can be expressed as

$$\varepsilon^* = \frac{1-S_{11}}{j\omega C_0 Z_0(1+S_{11})} - \frac{C_f}{C_0} \quad , \tag{14.7}$$

where $C_f$ is the fringing capacitance of the open-ended probe.

The most accurate determination of the permittivity from the reflection coefficient measurement occurs when

$$C_0 = \frac{1}{\omega Z_0\sqrt{\varepsilon'^2+\varepsilon''^2}} \quad , \tag{14.8}$$

provided that the uncertainties in the amplitude and phase $\varphi$ of the reflection coefficient are about the same i.e., $\Delta\varphi \approx |\Delta S_{11}/S_{11}|$. If the $C_f/C_0$ term in Equation (14.7) is neglected, the uncertainties in the permittivity and loss tangent are given by [12]

$$\frac{\Delta\epsilon'}{\varepsilon'} = \left\{\left(\frac{\Delta C_0}{C_0}\right)^2 + \left(\frac{\Delta Z_0}{Z_0}\right)^2 + \left(\frac{1-|S_{11}|^2}{1+2|S_{11}|\cos(\varphi)+|S_{11}|^2}\frac{|\Delta S_{11}|}{|S_{11}|}\right)^2 + \left(\frac{1-2|S_{11}|cos\varphi+|S_{11}|^2}{1+2|S_{11}|cos\varphi+|S_{11}|^2}\frac{\Delta\varphi}{tan\varphi}\right)^2\right\}^{1/2} \tag{14.9a}$$

$$\frac{\Delta\varepsilon''}{\varepsilon''} = \left\{\left(\frac{\Delta C_0}{C_0}\right)^2 + \left(\frac{\Delta Z_0}{Z_0}\right)^2 + \left(\frac{4|S_{11}|+2cos\varphi+2|S_{11}|^2cos\varphi}{(1-|S_{11}|^2)(1+2|S_{11}|cos\varphi+|S_{11}|^2)}\Delta|S_{11}|\right)^2 + \left(\frac{2|S_{11}|sin\varphi}{1+2|S_{11}|cos\varphi+|S_{11}|^2}\Delta\varphi\right)^2\right\}^{1/2} \quad (14.9b)$$

$$\frac{\Delta tan\delta}{tan\delta} = \left\{\left(\frac{\Delta\varphi}{tan\varphi}\right)^2 + \left(\frac{1+|S_{11}|^2}{1-|S_{11}|^2}\frac{|\Delta S_{11}|}{|S_{11}|}\right)^2\right\}^{1/2} \quad . \quad (14.9c)$$

Here, the uncertainty in the frequency has been neglected. The capacitances $C_0$ and $C_f$ can be determined from a measurement of the reflection coefficient $S_{11}$ made while the probe is inserted in a dielectric reference sample with known permittivity. If $C_f$ is equal to zero, $C_0$ is determined from

$$C_0 = \frac{-2|S_{11}|sin\varphi}{\omega Z_0\varepsilon'(1+2|S_{11}|cos\varphi+|S_{11}|^2)} \quad . \quad (14.10)$$

Alternatively, for non-zero $C_f$,

$$C_0 = \frac{1-2|S_{11}|}{\omega Z_0\varepsilon''(1+2|S_{11}|cos\varphi+|S_{11}|^2)} \quad (14.11)$$

and

$$C_f = \frac{-2|S_{11}|sin\varphi}{\omega Z_0(1\pm2|S_{11}|cos\varphi+|S_{11}|^2)} - \varepsilon' C_0 \quad . \quad (14.12)$$

To maximize the accuracy of $C_0$, the dielectric reference sample should display low loss. Distilled water, ethanol, and saline solutions of known molarity are examples of suitable reference materials.

An alternate approach to *in vivo* imaging is to keep the probe external to the sample of interest rather than insert it directly into the tissue [14]. A schematic of the experimental system and an equivalent probe circuit are shown in Fig. 14.2. This external, near-field imaging technique requires a modified description of the probe-sample interaction. The external probe is considered to be an electrically small antenna with dimension $D$ much smaller than the wavelength: $D << \lambda$. The probe is located at a small distance $z << \lambda$ from the sample surface. The sample surface is defined as the interface between the presumably homogeneous external space and the heterogeneous interior of the tissue. The inhomogeneous medium is represented by a complex permeability $\varepsilon^*$ that is a function of the distance $z$ from the interface. To increase the sensitivity of the antenna to material properties, a matching resonator circuit can be inserted in series with the probe. The matching circuit ensures that the minimum value of the reflection $S_{11}$ occurs at the resonance frequency of the resonator.

Figure 14.2 **Model of an external probe.** (a) Schematic of the external, radio-frequency probe antenna interacting with a sample. The height-dependent complex permittivity of the sample is $\varepsilon^*(z)$. (b) The corresponding transmission line equivalent probe circuit. The position that is labeled "*A*" in the schematic corresponds to the circuit nodes labeled "*A*" in the circuit diagram. Adapted from A. N. Reznik and N. V. Yurasova, *J. Appl. Phys.* **98** (2005) art. no. 114701., with permission from AIP Publishing.

As in the case of other near-field probes that we have described throughout the book, the presence of this medium will result in a change of the antenna's input impedance. Thus, the central problem for the external near-field probe is to calculate the change of the probe impedance due to perturbation by the sample with permittivity profile $\varepsilon^*(z)$. As shown in Fig. 14.2, a transmission-line-based approach can be used to model the system response. The probe is modeled through a parallel combination of an open ended line with length $l_s$ that serves as the matching circuit and a line of length $l_1$ that is loaded with the input impedance $Z_p$ of the probe. The characteristic impedance of these lines is $Z_l$ and propagation constant $\gamma_l = jk_l$ , where $k_l$ is corresponding wave number of the propagating wave. The lines are assumed to be lossless. The parallel combination of the probe and the matching circuit is fed by a line with characteristic source impedance $Z_0$. The feed line also serves as the detection path. The total input impedance of the circuit shown in Fig. 14.2(b) follows from standard transmission line theory and is

$$Z_{in} = \frac{Z_1 Z_2}{Z_1 + Z_2} \quad , \tag{14.13}$$

where

$$Z_1 = -jZ_l \cot(k_l l_s) \quad , \tag{14.14a}$$

$$Z_2 = Z_l \frac{Z_l - jZ_p cot(k_l l)}{Z_p - jZ_l cot(k_l l)} \quad . \tag{14.14b}$$

If the matching line is lossy, appropriate modifications have to be applied to the model. Note that Equations (14.14) depend upon the input impedance of the probe, including the effects of the sample properties and the interaction between the probe and the material. Simple forms of this impedance have been discussed for a variety of cases in Chapter 9. More complex expressions can be found in Reference [14] that take into account depth-dependent permeability and field distributions of the excited modes. As in the case of the inserted probe, the external near-field probe requires reference samples with known permittivity in order to obtain calibrated, quantitative measurements.

### *14.2.3 Multilayer systems*

Modeling the probe-sample impedance becomes more challenging for biological samples, most of which are hetereogeneous. For example, a more complex model for a two- or three-layer system representing the response of mammalian skin was presented in Reference [15]. In the two-layer model, the upper layer is a good conductor and represents the combined effects of the epidermis. The underlying second layer represents subcutaneous fat, which has a low dielectric constant. In the three-layer model, the epidermis is split into the stratum corneum and the dermis. The stratum corneum is about 30 micrometers thick and has a low dielectric constant. The dermis is about 1 mm to 2 mm thick and has a high dielectric constant. Following this modification, the third layer now represents the subcutaneous fat. The coupling of an external probe to this system is considered to be capacitive and may be analytically determined through a combination of the propagating TEM mode and evanescent TM modes, as discussed in Chapter 9. As we

show below, though the two- and three-layer models are conceptually simple, the analysis required to extract quantitative information from such a system is complex and challenging. Though the analysis below is framed in terms of the specific example of mammalian skin, this multilayer model form can be generalized to represent a variety of layered biological structures.

The problem at hand is to calculate the capacitance of a coaxial probe in contact with the layered biological medium. This capacitance is related to the effective permittivity (dielectric constant) through a simple relation $C_p = \varepsilon C_0$, where $C_0$ is once again the capacitance of the probe in free space. If the inner and outer conductors of the coaxial probe are $a$ and $b$, respectively, then this model applies only under the condition that $2a/\lambda << 1$. Clearly, this condition limits the frequency range within which this approach is valid. If it is assumed that the potential of the inner conductor of the coaxial probe is $V_0$, then the potential inside of the cable can be expresses as [15]

$$V_p(z,\rho) = V_0 \frac{\ln(\rho/b)}{ln(a/b)} + V_0 \sum_{i=1}^{N} g_i T_i(\rho) \exp(p_i z)\,; \qquad a \le \rho \le b \tag{14.15}$$

with

$$T_i(\rho) = A_i J_0(p_i \rho) + B_i Y_0(p_i \rho) \quad . \tag{14.16}$$

$J_0$ and $Y_0$ are Bessel functions of the first and second kind. The coefficients $A_i, B_i,$ and $p_i$ are determined from the boundary conditions $T_i(a) = T_i(b) = 0$ and the normalization condition $A_i^2 + B_i^2 = 1$. Each layer, indexed by n = 1, 2, … has potential $V_n$ and permittivity $\varepsilon_n$. To solve for $V_n$ in each layer for $z \ge 0$, it is necessary to solve a Laplace equation for a functions $f_n(z,\rho)$ related to $V_n$ through Hankel transformation [15]

$$f_n(z,\lambda) = \int_0^\infty V_n(z,\rho) J_0(\lambda\rho)\rho d\rho \quad . \tag{14.17}$$

The Laplace equation is then reduced to

$$\frac{\partial^2 f_n}{\partial z^2} - \lambda^2 f_n = 0 \quad . \tag{14.18}$$

Boundary conditions must be applied to ensure the continuity of the potential and the normal component of the electric displacement field at the boundaries of layers with thicknesses $d_1, d_2$ . For the three-layer structure, the boundary conditions are

$$f_1 = f_2 \qquad \varepsilon_1 \frac{\partial f_1}{\partial z} = \varepsilon_2 \frac{\partial f_2}{\partial z} \qquad at\ \ z = d_1$$

$$f_2 = f_3 \qquad \varepsilon_2 \frac{\partial f_2}{\partial z} = \varepsilon_3 \frac{\partial f_3}{\partial z} \qquad at\ \ z = d_1 + d_2 \tag{14.19}$$

Solving (14.18) with boundary conditions (14.19) leads to [15]

$$f_1(z,\lambda) = f_0(\lambda) \frac{e^{-\lambda z} + e^{\lambda z} R_t exp(-2\lambda d_1)}{D_1} \quad , \tag{14.20}$$

$$f_2(z,\lambda) = f_0(\lambda)(1+R_t)\frac{e^{-\lambda z}+e^{\lambda z}R_2 exp(-2\lambda(d_1+d_2))}{D_1 D_2} \quad , \tag{14.21}$$

and

$$f_3(z,\lambda) = f_0(\lambda)(1+R_t)(R_2+1)\frac{e^{-\lambda z}}{D_1 D_2} \quad . \tag{14.22}$$

Here

$$D_1 = 1 + R_t exp(-2\lambda d_1); \qquad D_2 = 1 + R_2 exp(-2\lambda d_2) \tag{14.23}$$

and

$$R_t = \frac{R_1+R_2 exp(-2\lambda d_2)}{1+R_1 R_2 exp(-2\lambda d_2)}; \quad R_1 = \frac{\varepsilon_1-\varepsilon_2}{\varepsilon_1+\varepsilon_2}; \quad R_2 = \frac{\varepsilon_2-\varepsilon_3}{\varepsilon_2+\varepsilon_3} \tag{14.24}$$

Following Reference [15] and references therein, it is possible to derive the relation

$$f_0(\lambda) = F_0(\lambda) + \sum_{i=1}^{N} g_i F_i(\lambda) \quad , \tag{14.25}$$

where

$$F_0(\lambda) = \frac{V_0}{\lambda^2 ln(b/a)}(J_0(\lambda b) - J_0(\lambda a)) \tag{14.26}$$

and

$$F_i(\lambda) = \frac{V_0 p_i}{p_i^2-\lambda^2}[bJ_0(\lambda b)(A_i J_1(p_i b) + B_i Y_1(p_i b) - aJ_0(\lambda a)(A_i J_1(p_i a) + B_i Y_1(p_i a))] \quad . \tag{14.27}$$

The capacitance of the probe can be expressed through the variation formula

$$\frac{C_p}{\varepsilon_0} = \frac{2\pi\varepsilon_1}{V_0^2}\sum_{i=0}^{N} g_i \sum_{j=0}^{N} g_j P_{ij} + 2\pi\varepsilon_t \sum_{i=1}^{N} g_i^2 p_i t_i \quad , \tag{14.28}$$

where

$$P_{ij} = \int_0^\infty F_i(\lambda)F_j(\lambda)\frac{1-R_t(\lambda)exp(-2\lambda d_1)}{1+R_t(\lambda)exp(-2\lambda d_1)}\lambda^2 d\lambda \tag{14.29}$$

and

$$t_i = \int_a^b T_i^2(\rho)\rho d\rho \quad . \tag{14.30}$$

In the sums in Equation (14.28), $g_0$ =1 and $\varepsilon_t$ is the permittivity of the dielectric in the coaxial cable.

To get the coefficients $g_i$ it is necessary to solve (approximately) the second boundary condition

$$\varepsilon_1 \frac{\partial V_1}{\partial z} = \varepsilon_t \frac{\partial V_t}{\partial z} \quad , \; z = 0 \; and \; a \le \rho \le b \tag{14.31}$$

For *N*=3 e.g., this leads to set of equations for g coefficients

$$P_{01} + g_1 P_{11} + g_2 P_{12} + g_3 P_{13} = -V_0^2 \frac{\varepsilon_t}{\varepsilon_1} g_1 p_1 t_1 \quad , \tag{14.32a}$$

$$P_{02} + g_1 P_{21} + g_2 P_{22} + g_3 P_{23} = -V_0^2 \frac{\varepsilon_t}{\varepsilon_1} g_2 p_2 t_2 \quad , \tag{14.32b}$$

$$P_{03} + g_1 P_{31} + g_2 P_{32} + g_3 P_{33} = -V_0^2 \frac{\varepsilon_t}{\varepsilon_1} g_3 p_3 t_3 \quad . \tag{14.32c}$$

Similarly, the capacitance for *N*=2 can be written as

$$\frac{C_p}{\varepsilon_0} = \frac{1}{V_0^2} 2\pi\varepsilon_1 (P_{00} + 2g_1 P_{01} + 2g_2 P_{02} + 2g_1 g_2 P_{21} + g_1^2 P_{11} + g_2^2 P_{22}) + 2\pi\varepsilon_t \sum_{i=1}^{2} g_i^2 p_i t_i \tag{14.33}$$

The solution of these equations requires the numerical evaluation of the integrals in Equation (14.29), which is nontrivial. For some simpler cases, approximate formulae can be used. For a bilayer structure the permittivity seen by the probe can be approximated as

$$\varepsilon_p = (\varepsilon_1 - \varepsilon_2)\left(1 - e^{-qd}\right) + \varepsilon_2 \quad , \ \varepsilon_1 > \varepsilon_2 \tag{14.34}$$

or

$$\frac{1}{\varepsilon_p} = \left(\frac{1}{\varepsilon_1} - \frac{1}{\varepsilon_2}\right)\left(1 - e^{-qd}\right) + \frac{1}{\varepsilon_2} \quad , \ \varepsilon_1 < \varepsilon_2 \quad . \tag{14.35}$$

In Equations (14.34) and (14.35), $q$ is a constant that depends on the probe size. These equations can be extended for the three-layer skin model with $\varepsilon_1 < \varepsilon_2$ and $\varepsilon_2 > \varepsilon_3$. It is useful for the three-layer case to distinguish the adjustable constants for stratum corneum $q = q_{sc}$ and epidermis/dermis $q = q_{ed}$. One can then write

$$\varepsilon_{d+sf} = \varepsilon_d[1 - \exp(-q_d d_d)] + \varepsilon_{sf}\exp(-q_d d_d) \tag{14.36}$$

and

$$\frac{1}{\varepsilon_p} = \frac{1-\exp(-q_{sc} d_{sc})}{\varepsilon_{sc}} + \frac{\exp(-q_{sc} d_{sc})}{\varepsilon_d[1-\exp(-q_d d_d)] + \varepsilon_{sf}\exp(-q_d d_d)} \quad . \tag{14.37}$$

The indices *sc*, *d* and *sf* correspond to stratum corneum, dermis and fat layers.

Though the mathematical details of this example are somewhat complex, it is important to stress that the objective is conceptually simple. In general, the interaction of the probe with the sample is modeled by calculating an impedance. In this particular case, as in most cases where a dielectric sample is being characterized at microwave frequencies, the task is further simplified to a calculation of a capacitance, as in Equations (14.28) and (14.33) above.

### *14.2.4 Heterogeneous, liquid systems*

Having established a framework for modeling the electromagnetic probe-sample interaction and having applied that framework to the particular case of multilayer systems, we turn to characterization of

heterogeneous, biological systems in a liquid environment. Quantitative measurement of local electromagnetic properties within a liquid environment by use of a coaxial cavity was addressed in Reference [16]. As with several other resonant-cavity-based systems discussed throughout this book, the measured parameters are the shift of the resonance frequency and the change in the quality factor. Once again, these changes are quantitatively related to the presence of the sample material within the near field of the probe. In a physiological, liquid environment, further consideration must be given to the dielectric description of the biological tissue, including various relaxation phenomena and water binding. Reference [16] was among the first to address the fact that the application of higher frequencies enables separate extraction of the free water relaxation. In addition, in cases where an inclusion is present in a host sample medium, the mixture may be described by an effective permittivity given by the Maxwell-Garnett mixing formula [17]

$$\varepsilon_{eff} = \varepsilon_h + f_V \varepsilon_h \frac{\varepsilon_i - \varepsilon_h}{\varepsilon_h + (1-f)(\varepsilon_i - \varepsilon_h)} \quad , \tag{14.38}$$

where $\varepsilon_h$ is the permittivity of the host, $\varepsilon_i$ is the permittivity of the inclusion and $f_V$ is the fraction of the total volume of the inclusion. Many biological media consist of two components: a dry component with permittivity $\varepsilon_i$ and water with permittivity $\varepsilon_w$. In this case, the permittivity of such a mixture satisfies the relationship [18]

$$V_w \frac{\varepsilon_w(f_V,T,S) - \varepsilon_{eff}}{\varepsilon_w(f_V,T,S) + 2\varepsilon_{eff}} + (1 - V_w)\frac{\varepsilon_i - \varepsilon_{eff}}{\varepsilon_i + \varepsilon_{eff}} = 0 \quad . \tag{14.39}$$

Here, $V_w$ is the volume of the water. The relative permittivity of the water is a function of the frequency, temperature and salinity. It can be calculated from [19]

$$\varepsilon_w = \varepsilon_\infty + \frac{\varepsilon_s(T,S) - \varepsilon_\infty}{1 + j\omega\tau(T,S)} - j\frac{\sigma(T,S)}{\omega\varepsilon_0} \quad , \tag{14.40}$$

where $\varepsilon_0$ is the permittivity of vacuum and $\varepsilon_\infty = 4.9$ is the relative permittivity of the water at optical frequencies. Formulas for the static permittivity $\varepsilon_s$, relaxation time $\tau$ and conductivity $\sigma$ as a function of temperature *T* and salinity *S* can be found in the literature [19].

Though effective dielectric constants can be important in determining the structure and the thermodynamics of electrostatically interacting systems under different electrostatic conditions, it is difficult to isolate and estimate the dielectric constant of specific constituent parts of biological macromolecules such DNA when they are embedded in a host environment. This estimation is further complicated due to the presence of ions in the system. At low ion concentration, the problem can be reduced to an analysis of Coulomb forces. At high ion concentration, the interactions can only be described numerically by calculations that include correlations. The ions' influence on the dielectric constant in turn influences the resulting forces and the Debye screening length. In this process, one has to distinguish between the static dielectric constant of the solution and the static dielectric constant of the solvent.

Thus, when describing the dielectric constant of biological macromolecules in an ionic solution, it may be necessary to include the statistical behavior of the system. One reasonable approach is to separate the

overall dielectric constant into self-terms for individual components (component dielectric constants) and cross-terms between components. This approach is well defined mathematically. Reference [20] showed that the cross-terms are negligible compared to the self-terms when the components are grouped appropriately. Although the dielectric constant of an inhomogeneous system is an aggregate property combining the effects of all the constituents of the system, it is possible to separately calculate the contributions of a macromolecule and the solvent to the total dielectric constant by use of molecular dynamics simulations. Furthermore, such simulations enable the evaluation of any cross-terms, should they be non-negligible. The analysis underlying such simulations is as follows. The dielectric constant of a system ε surrounded by an infinite dielectric medium with a dielectric constant $\varepsilon_e$ is related to dipole fluctuations by [20]

$$\frac{(\varepsilon-1)(2\varepsilon_e+1)}{(2\varepsilon_e+\varepsilon)} = \frac{\langle\vec{M}^2\rangle-\langle\vec{M}\rangle^2}{3\varepsilon_0 V k_B T} = \alpha \quad . \tag{14.41}$$

$\vec{M}$, and *V*, and *T* are the total dipole moment, the volume, and the temperature of the system, respectively. Two special cases are of interest. First, as $\varepsilon_e \to \infty$ then

$$\varepsilon_1 = 1 + \alpha \quad , \tag{14.42}$$

where $\varepsilon_1$ is the dielectric constant of the system. Second, when $\varepsilon_e = \varepsilon$ then

$$\varepsilon_2 = \frac{1}{4}(3\alpha + 1 + \sqrt{9\alpha^2 + 6\alpha + 9}) \tag{14.43}$$

where $\varepsilon_2$ is dielectric constant of the system.

The total dipole moment of a system of N particles is defined as

$$\vec{M} = \sum_{i=1}^{N} q_i \vec{r_i} \tag{14.44}$$

where $q_i$ is the partial charge and $\vec{r_i}$ is the position vector of the *ith* particle. For a system composed of particles of *m* different groups it is possible to decompose $\vec{M}$ into m components

$$\vec{M} = \sum_{k=1}^{m} \overrightarrow{M_k} \text{ with } \overrightarrow{M_k} = \sum_{i=N_{k-1}+1}^{N_{k-1}+n_k} q_i \vec{r_i} \quad . \tag{14.45}$$

Here $n_k$ is the number of particles in group *k* and $N_k = \sum_{l=1}^{k} n_l$. Following this decomposition, the mean square deviation of dipole moment can be expressed as

$$\Delta(\vec{M}) = \langle\vec{M}^2\rangle - \langle\vec{M}\rangle^2 = \sum_{k=1}^{m}\left(\langle\vec{M}_k^2\rangle - \langle\vec{M}_k\rangle^2\right) + 2\sum_{l=k+1}^{m}\sum_{k=1}^{m}\left(\langle\vec{M}_k \cdot \vec{M}_l\rangle - \langle\vec{M}_k\rangle \cdot \langle\vec{M}_l\rangle\right) \quad . \tag{14.46}$$

This formulation can be used to calculate the dielectric constant of many complex systems. For example, it was used in [21] to calculate the internal dielectric constant of DNA through molecular dynamic calculations.

## 14.3 Electrical scanning probe microscopy of biological systems

### *14.3.1 General considerations*

Ideally, electrical scanning-probe measurements are carried out under experimental conditions that match physiological conditions [22]. In order to characterize fragile biological systems such as soft membranes and molecular complexes in their native environments, AFMs are often operated in “gentler” modes, such as dynamic force microscopy. Dynamic microscopy modes are usually less destructive than direct contact mode, but require driven mechanical oscillation of the cantilever or sample. For example, an external magnetic field may be used to drive the oscillation of a cantilever in a solution. Dynamic microscopy modes provide a rich set of information. Measurements of the phase of the cantilever oscillations and measurements of higher order vibrational modes of the cantilever reveal features of the investigated material that can’t be obtained from topographic images alone. In many cases, the immobilization of objects on a surface is critical to AFM imaging. This requires proper selection of the substrate as well as careful attention to electrical charging of the surface. Mica is a commonly used substrate for this purpose, as it is smooth and easy to cut. Furthermore, its surface is can be modified to be either positively or negatively charged and thus can be used to immobilize both negatively and positively charged samples.

Below, we focus primarily on electrical scanning probe microscopy, but scanning-probe-based, mechanical measurement techniques are also important for life sciences metrology. For example, monitoring the inter- and intra-molecular forces is an area where the application of AFM has proven to be quite useful. Molecular-scale force measurements provide insight about structure dynamics within investigates species. The range of these forces is from several femtoNewtons to several nanoNewtons, roughly corresponding to the forces necessary to rupture of covalent bonds.

### *14.3.2 Electrostatic force microscopy*

Numerous electrical, AFM-based metrology tools, such as scanning electrochemical microscopy and spreading resistance microscopy, are based on the measurement of electric currents. Others, such as electrostatic force microscopy and Kelvin probe microscopy, are based on the measurement of induced electrostatic forces. Each of these techniques provides valuable, complementary insight into electronic and transport properties of material systems. In the specific application of these techniques to biological objects, measurement in a relatively low-frequency regime requires capacitance measurements with sub-attofarrad sensitivity. In addition, such measurements may be complicated by operation in a liquid environment. There are very few experimental techniques that can fulfill these experimental requirements.

One such technique is amplitude-modulated, electrostatic force microscopy (AM-EFM), which is a slight modification to conventional EFM that operates at MHz frequencies and allows dielectric imaging in liquid media with nanoscale spatial resolution [23]. The critical aspect of this approach is that the application of a tip voltage at frequencies above 1 MHz introduces a strong electrostatic force at the apex of the probe,

which is sensitive to local dielectric properties of the sample under study. At the lower operating frequencies typically used in conventional EFM, non-local contributions from the cantilever and other supporting structures are sensed in addition to the localized contribution from the probe tip. The measured force is exerted by a sinusoidal voltage $v(t) = V_{ac}\cos(\omega t)$ between the tip and the bottom of the sample and is given by

$$F_{els}(z,t) = \frac{1}{2}\frac{dC}{dz}V_{ac}^2(\cos(\omega t))^2 = -\frac{1}{4}\frac{dC}{dz}V_{ac}^2 + \frac{1}{4}\frac{dC}{dz}V_{ac}^2\cos(2\omega t) \quad . \quad (14.47)$$

For excitation frequencies greater than 1 MHz that are well beyond the resonance frequency of the cantilever only the first term on the right-hand side of Equation (14.47) can be detected as a static bending of the cantilever, which depends on the excitation amplitude $V_{ac}$. To improve detection accuracy, the signal amplitude is modulated by $V_{ac}(t) = V_0\cos(\omega_{mod}t)$. By use of a lock-in amplifier, one can measure the effective capacitance gradient

$$\frac{dC}{dz} = 4|F_{els}(z,t)|_{f_{mod}}/V_0^2 \quad , \quad (14.48)$$

where $V_0$ is the amplitude of the modulation signal, $f_{mod}$ is the frequency of the modulated signal typically set to a few kHz, *z* is the tip-sample distance, and *t* is time. Importantly, the effective capacitance gradient depends on the frequency, solution conductivity and the dielectric properties of the sample.

Figure 14.3. **Models of an electrostatic force microscope operating in liquid.** (a) Schematic of the tip-solution-sample system, including the tip apex, electrochemical double layers (EDLs), bulk solution, and sample. (b) Equivalent electric circuit model for the system. (c) Simplified electric circuit model [23]. 

A qualitative physical understanding of AM-EFM be obtained from an equivalent circuit model in which a simple parallel plate model represents the tip-sample system in one dimension [23]. A schematic of this model is shown in Fig. 14.3(a) and a corresponding equivalent circuit model is shown in Fig. 14.3(b). The model accounts for the capacitance and resistance of the solution, the sample capacitance, $C_{smpl}$, and the double layer capacitance(s), $C_{dl}$, that may form close to the electrodes in the solution. This model can be further simplified if the double layer and sample capacitances are combined into an equivalent capacitance $C_{eq}$, as it is shown in Fig. 14.3(c) (Note, that typically $C_{dl}$ can be also neglected since it is much larger than and in series with $C_{smpl}$). The capacitance and resistance values can be calculated from the corresponding material properties by $C_{smpl} = \varepsilon_0\varepsilon_{r,smpl}/h$, $C_{sol} = \varepsilon_0\varepsilon_{r,sol}/z$ and $R_{sol} = \frac{z}{\Lambda c}$ where $\Lambda$ is the molar conductivity, *c* is the salt concentration, $\varepsilon_{r,i}$ are the relative permitivities of the solution and the sample, *z* is the tip-sample distance, *h* is the sample thickness and $\varepsilon_0$ is the permittivity of free space. Following the simplified model in Fig. 14.3(c), the electrostatic force can be expressed as [23]:

$$[F_{els}(z,f)]_{f_{mod}} \approx \frac{1}{4}\frac{\varepsilon_0\varepsilon_{r,sol}f^2\left(\frac{2\pi\varepsilon_0\varepsilon_{r,smpl}}{\Lambda ch}\right)^2}{1+f^2\left(\frac{2\pi\varepsilon_0\varepsilon_{r,smpl}z}{\Lambda ch}+\frac{2\pi\varepsilon_0\varepsilon_{r,sol}}{\Lambda c}\right)^2}V_0^2 \quad . \tag{14.49}$$

The force depends strongly on frequency. The practical implication of this is that the force can only be at frequencies above a certain actuation frequency, which is given by [24]:

$$f_{act} = \frac{c\Lambda}{2\pi\varepsilon_0\varepsilon_{r,sol}}\left(\frac{\varepsilon_{r,smpl}z}{\varepsilon_{r,sol}h}+1\right)^{-1} \quad . \tag{14.50}$$

For an ideal case of a pure dielectric solution ($c$ = 0), Equation (14.49) becomes independent of the frequency and $f_{act}=0$. Note that $f_{act}$ is dependent on the tip-sample distance $z$. Thus, changes in the probe-sample separation will require a corresponding change in the excitation frequency in order for the the local tip apex force to be detected [23]. Another important implication of Equation (14.49) is that electrostatic force rises much slower with decreasing $z$ in liquid compared to air. Finally, though the parallel-plate model gives valuable qualitative insights, comparison to finite-element modelling is required for accurate, quantitative interpretation of measurements and estimation of material parameters [25].

### *14.3.3 Near field scanning microwave microscopy of biological systems*

Measurements of the electromagnetic properties of single cells at frequencies in the microwave and millimeter-wave ranges are important for microwave-frequency-based diagnostics and therapies. Furthermore, such measurements provide insight into potentially hazardous influences of microwave radiation on biological material. One electromagnetic material parameter that captures many characteristics of biological specimens is complex permittivity. From an experimental point of view, there is particular interest in the measurement of transmission, reflection and absorption of microwave radiation by biological materials, such as tissue, cells, proteins, and bacteria. Up to now, most measurements of the complex permittivity of biological materials have been enabled by integrating the sample with microelectrodes or microfluidic devices. The resolution of such approaches is inherently limited at small length scales and falls short of the subcellular level. NSMM offers an alternative, non-destructive experimental approach for accessing the electromagnetic properties of biological samples with high spatial resolution. One further advantage of NSMM is that the penetration depth of microwaves into these materials is significant. Therefore, the technique offers a unique opportunity to simultaneously produce high resolution maps of both surface and subsurface electromagnetic properties.

One area where NSMM is especially useful is the characterization of samples that combine cells or other soft matter with artificial nanostructures. One of the first applications of evanescent microwaves as a nondestructive, high-resolution imaging technique for biological systems was pioneered by Wei [26]. This was followed by the work Tabib-Azar [27], which pushed the spatial resolution from about 5 μm to λ/750,000, which corresponds to 0.4 μm at 1 GHz and 0.04 μm at 10 GHz. This early work clearly

demonstrated the capability to measure biological and botanical specimens with NSMM. Since this early work, the development of NSMM techniques for biological applications has grown significantly.

*14.3.4 Topographic artifacts in microwave microscopy*

In addition to addressing the challenges of operation in a heterogeneous, liquid environment, it is necessary to address the convolution of topographic effects with material measurements during NSMM measurements. This is a general challenge to NSMM image interpretation and is not limited to biological materials. As the probe is scanned over nonuniform topography, changes in the probe-sample distance and the sample curvature modify the probe-sample capacitance. Thus, overall changes to the probe-sample capacitance represent the combination of changes due to geometry and changes of the electromagnetic properties of the investigated material. As a result, the geometrical contribution can mask the local dielectric response. It is an important challenge that has to be met in order for NSMM to be an effective technique for the quantitative characterization of materials and devices. Research into this problem is ongoing, but there are several approaches that can be used to mitigate this problem, though none of them is universal.

Reference [22] addresses the topography "cross talk" problem for nonplanar, biological samples, namely the single *E.coli* bacterial cells. The objective is to remove the effects of topography in order to measure the nanoscale permittivity of a single cell. The first step is to calculate theoretical NSMM capacitance images using numerical, three-dimensional methods that account for the tip-sample geometry as well as the electromagnetic material properties. The model assumes that the tip possesses a spherical apex and that the cell is an ellipsoid with uniform relative permittivity $\varepsilon_r$. As a first approximation, this approach gives a reasonable estimate of the geometrical contribution to the capacitance. Within such a model, it is possible to generate simulated NSMM images through numerically calculated, virtual scans at a constant tip-sample distance. Fig. 14.4(a) shows such a virtual scan over a single cell with $\varepsilon_r$ =4.0. Fig. 14.4(b) shows a calculated line scan for the same bacterial cell. The calculation illustrates that when the tip is moving over the bacterial cell there is a significant decrease in the capacitance due to increased distance between the tip and the underlying substrate. This example also demonstrates that the contribution of the topography-dependent capacitance dominates the contribution of the dielectric response of the sample, especially for small tip apex sizes below 100 nm. Such a complication is common in NSMM capacitance images of soft, dielectric matter. Special design of the probes and their shielding will mitigate but not completely remove this contribution. To obtain the intrinsic dielectric response of the sample, the topographic cross-talk contribution has to be subtracted from the measured capacitance image as shown in Fig. 14.4(c). At present, this approach represents a practical route to local, topography-free, quantitative permittivity characterization.

Figure 14.4. **Topographic contribution to an image of a bacteria cell.** (a) Virtual scan image of a bacterial cell (relative permittivity $\varepsilon_r$=4) generated by use of a numerical simulation. (b) Transverse line scan across the virtual image in (a), representing the modeled topographic "cross-talk" in the NSMM image. (c)

Measured NSMM line scan (raw), modeled topographic contribution (cross-talk), and the difference between the measured data and the topographic contribution (intrinsic). Adapted with permission from M. Ch. Biagi, R. Fabregas, G. Gramse, M. Van Der Hofstadt, A. Juárez,F. Kienberger, L. Fumagalli, and G. Gomila, *ACS Nano* **10** (2016) pp.280-288. Copyright 2016, American Chemical Society.

An alternative approach to removal of the topographic cross-talk is based on the use of measured experimental data in conjunction with an empirical model. This approach does not require *a priori* numerical modeling based on system geometry. The topography-dependent contribution to the measured reflection signal $S_{11}$ is approximated by selecting a sub-region of an image within which the material properties are known not to vary. The difference between the measured and predicted values represents an estimate of the contribution due to material property variations alone.

The empirical model approach is demonstrated with representative NSMM images of a GaN nanowire shown in Fig. 14.5. A topographic image and an image of the magnitude of the raw reflection coefficient $S_{11}$ are shown in Figs. 14.5(a) and 14.5(b), respectively. Fig. 14.5(c) shows an $S_{11}$ image that has been post-processed to reduce noise and other artifacts. Based on a selected sub-region of the topography and processed $S_{11}$ images, a scatterplot of topography and $S_{11}$ is generated, as shown in Fig. 14.5(d). The sub-region of the imaged area that was chosen to generate the scatterplot in Fig. 14.5(d) is expected to have little, if any material contrast. In this case, this sub-region is topographically-smooth, but sample tilt and long-range sample curvature lead to variability in the as-measured topography. The black crosses in the scatterplot represent the experimental data while the gray circles represent an empirical model that relates the topography to the reflection coefficient based on the overall trend in the experimental data. Fig. 14.5(e) shows topographic (dashed line) and reflection coefficient (solid line) line cuts through the nanowire from the processed image. Fig.14.5(f) compares the processed reflection coefficient measurement (solid line) to the extracted reflection coefficient that is based on the empirical model derived from the scatterplot. Note that the predicted reflection coefficient displays the same magnitude in the areas around the nanowire, which is consistent with material-independent, purely geometrical features. The difference between the predicted and measured reflection coefficient is shown in Fig. 14.5(g). The displayed difference represents an estimate of the materials-dependent contribution to the $S_{11}$ measurement. A more precise model can be developed by complementing the empirical model with a physical description that incorporates the material parameters within the sub-region of the image: relative effective permittivity, conductivity and loss. Ideally, these material parameters are constant within a well-chosen sub-region and would result only in an offset of the materials-dependent contribution to the reflection coefficient.

Figure 14.5 **Empirical procedure to de-embed the topography from $S_{11}$ in near-field scanning microwave microscope images.** (a) Topographic image, (b) as-measured $S_{11}$ image, and (c) processed $S_{11}$ image of a GaN nanowire. (d) Scatterplot relating the topographic measurements from (a) to the $S_{11}$ measurements in a sub-section of the image (black plus symbols). The empirically observed trend in the data is shown

(grey circles). (e) Line cuts of the measured topography (Topo) and the processed $S_{11}$ image. The position of the line cuts is shown by a dashed line in the images. (f) Comparison of the $S_{11}$ line scan to the predicted topographic contribution to the line scan (Pred). The topographic contribution is predicted from the trend shown in (d). (g) The difference (Diff) between the measured $S_{11}$ line scan and the estimated topographic contribution.

As alluded to in the preceding discussion, another important aspect of NSMM data interpretation is processing and de-noising of measured data. The overall processing procedure should level the image, correct for scan offsets, and reduce noise in the images. One method for such processing is introduced in Reference [28], is based on estimating the difference between the ideal, noiseless reflection coefficients $\rho(x, y, f_0)$ and the measured reflection coefficient $\Gamma(\mathrm{x}, \mathrm{y}, \mathrm{f}_0)$. Both $\rho$ and Γ are functions of the probe position and NSMM operating frequency. Moreover,

$$\rho(x, y, f_0) = \rho(\Gamma(\mathrm{x}, \mathrm{y}, \mathrm{f}_0)) \quad . \tag{14.51}$$

If we assume that the measured reflection coefficient can be expressed as

$$\Gamma(\mathrm{x}, \mathrm{y}, \mathrm{f}) = \Gamma_0(f) + Er(x, y, f);\ Er \ll \Gamma_0 \quad , \tag{14.52}$$

then it is possible to expand $\rho$ into Taylor series

$$\rho(\Gamma) = \rho(\Gamma_0) + \frac{\partial \rho}{\partial \Gamma}\Big|_{\Gamma=\Gamma_0} Er(f) = G(f)I(x, y, f) + \rho_0(f) \quad . \tag{14.53}$$

Equation (14.53) represents a general case where the *I* is any image representation, $\rho_0$ represents the translation of the reflection coefficient, *G(f)* is a "gain" one needs to adjust the image representation, and *Er*(*f*) represents the small variations of the reflection coefficient due to small spatial variations of essentially the tip-to-sample capacitance.

Next, for practical measurements, it is reasonable to assume that the measured quantity $\rho$ is affected by some noise. Then, Equation (14.53) is modified to

$$\rho'(x, y, f_0) \cong G(f)I(x, y, f) + n(x, y, f_0) + \rho_0(f_0) \quad , \tag{14.54}$$

where $n(x, y, f_0)$ represents the noise. This noise can come from many different sources, including the random mechanical vibrations of the tip, that in turn cause the variation of the tip-sample capacitance. The noise contribution is assumed to have a mean of zero when averaged over all space. To reduce the noise contribution, a set of measurements is performed with the NSMM operating frequency in the vicinity of the nominal operating frequency $f_0$: $f = f_0 + \Delta f$. Further, it is assumed that there is not a significant change in the imaged variable around $f_0$, which is a reasonable assumption for most NSMM measurements. Equation (14.54) becomes

$$\rho'(x, y, f_k) \cong G(f_k)I(x, y, f_0) + n(x, y, f_k) + \rho_0(f_k) \quad . \tag{14.55}$$

The set of measurements is indexed by $k = 1,2 \ldots N$. For each of these measurements it is possible to calculate a spatial average

$$\overline{\rho_0}(f_k) \cong G(f_k)(\langle I(x,y,f_0)\rangle) + \rho_0(f_k) \tag{14.56}$$

and calculate the difference

$$\rho'(x,y,f_k) - \overline{\rho_0}(f_k) \cong G(f_k)(I(x,y,f_0) - \langle I(x,y,f_0)\rangle + n(x,y,f_k)) \quad . \tag{14.57}$$

To make this quantity independent of gain, it is necessary to divide Equation (14.57) by $G(f_k)$ and average over the frequency range to recover

$$\langle \frac{\rho'(x,y,f_k) - \overline{\rho_0}(f_k)}{G(f_k)} \rangle_f \cong I(x,y,f_0) - \langle I(x,y,f_0)\rangle \tag{14.58}$$

Thus the measurement average is removed and the noise in the data is reduced.

Another approach for de-noising and de-trending NSMM images was presented in Reference [29]. This approach is based on robust and adaptive implementation of local regression together with local likelihood models. The basic idea of this approach is to adaptively select the size of the neighborhood about any point of interest and the associated weight in that neighborhood. This method is flexible in that it does not require the explicit knowledge of a global parametric model. In place of a global model that applies to the entire image, a local model is used fit to a neighborhood about each location of interest. The method utilizes the local regression method LOCFIT [30] to smooth and de-trend the images. Subsequent de-noising of the images is performed by use of Adaptive Weight Smoothing (AWS). AWS is also a local likelihood method in which the local models are fit by a weighted likelihood approach. Because the value of the weight can be zero, the method also preserves sharp features while suppressing additive noise in the regions where the image is smooth. The down weighting of large residuals is done by minimizing a cost function. The scan artifacts are suppressed by subtracting the median measured value in the given scan line. The de-noising is then done through suppression of artifacts by AWS where the weighted likelihood function at point *x* is modeled as

$$L(W(x),\theta) = \sum_i w_i(x)\log(p(Y_i,\theta)) \quad , \tag{14.59}$$

where $Y_i$ is measured at $x_i$, $w_i$ is the weight corresponding to the measured at $x_i$ and the point of interest at *x*, and *p* is the likelihood of $Y_i$ given the model parameter factor $\theta$.

### *14.3.5 Scanning probe microscopy at the cellular level*

We return now to characterization of biological samples with NSMM. As of this writing, some examples of NSMM images of biological samples have been reported, but the field remains in its infancy. In some cases, the object of interest may be difficult to resolve by raw reflection coefficient measurements. It may be more suitable to convert the reflection coefficient into calibrated complex admittance or impedance images that represent the sample conductance and capacitance, respectively [31]. Fig. 14.6 shows NSMM imaging of an *E.coli* bacterial cell [22]. Taken together, the results in Fig. 14.6 constitute the quantitative characterization of local permittivity of a single bacterial cell and demonstrate that microwave microscopy has the potential for nanoscale, label-free imaging of cells with high spatial resolution.

Figure 14.6 **Near-field scanning microwave microscopy of a bacterial cell.** (a) Topography, (b) calibrated capacitance, and (c) estimated topographic cross-talk images for the same bacterial cell in Figure 14.4. (d) Change in probe-sample as a function of tip height as the tip approaches a metallic sample. The curve has been offset in order to level it with the background substrate capacitance in the image. (d) Inset: topographic cross-section profile along the line in (a). (e) Intrinsic capacitance image, as determined by the process illustrated in Fig. 14.4. (f) Transverse line cuts referenced to the substrate and taken along the dashed lines in (b), (c), and (e). Reprinted with permission from M. Ch. Biagi, R. Fabregas, G. Gramse, M. Van Der Hofstadt, A. Juárez, F. Kienberger, L. Fumagalli, and G. Gomila, *ACS Nano* **10** (2016) pp.280-288. Copyright 2016, American Chemical Society.

The combination of STM with broadband scanning microwave microscopy for biological applications was investigated in References [32] and [33]. STM was chosen as the imaging platform due to its atomic-scale spatial resolution. In addition, STM is inherently a noncontact technique, which prevents deterioration of the tip. Conventional STM can be used only with conducting substrates, though an STM feedback mechanism based on RF signals was demonstrated in Reference [34], offering the possibility to extend this approach to non-conducting materials. The STM tip is capacitively coupled with the broadband and does not rely on a resonant cavity. As in conventional STM, a feedback loop keeps the probe at a constant distance from the sample by adjusting the height to keep the tunneling current constant. The combined STM-microwave microscope simultaneously images the topography and the reflection coefficient.

To calibrate STM-based microwave microscopes, three arbitrary, but known loads are measured [32], [33]. The error matrix model is shown in Fig. 14.7(a). It differs from the one-port calibration procedure discussed in Chapter 7 in that the unknown error admittance matrix $[Y_e]$ is considered to be a two-port circuit positioned between the tip and the microwave source. The tip is considered to be a sphere with the calibration reference plane crossing the center of the sphere, as shown in Fig. 14.7(b). Note that single mode propagation is assumed. In the case of strong sample-tip interactions there could be far field contributions and one would have to apply a multimode approach. Furthermore, due to the chosen position of the reference plane, the lower half of the tip sphere also contributes to the measured response of the sample. In principle, one could choose the reference plane at the very bottom of the sphere. The choice of the reference plane position is arbitrary, but not inconsequential in that it does not influence the calibration procedure, but does determine which parts of the test platform are embedded with the sample properties in the calibrated, measured images. If it is assumed that the error admittance matrix is reciprocal, then only three known loads are required to fully characterize the matrix elements. One way to produce three different loads is to perform measurements at three different heights of the tip above the sample. An image of an individual sarcomere obtained by use of this calibrated, STM-based microscope is shown in Fig. 14.7(c). The actin in I-band and myosin in the A-band possess different densities and thicknesses, leading to the banded appearance of features in Fig. 14.7(c) [35] .

Figure 14.7 **Radio-frequency scanning tunneling microscopy of a sarcomere.** (a) Schematic of the error matrix $Y^{(e)}$ positioned between the source and the STM-based, RF probe. (b) Reference plane position ($R$). The tip is assumed to terminate in a sphere and the reference plane crosses the center of the sphere. © 2011 IEEE. Adapted, with permission from M. Farina, D. Mencarelli, A. Di Donato, G. Venanzoni, and A. Morini, *IEEE Trans. Microw. Theory Techn.* **59** (2011) pp. 2769-2776. (c) RF STM image of a sarcomere. © 2015 IEEE. Reprinted, with permission from M. Farina, A. Di Donato, D. Mencarelli, G. Venanzoni, A. Morini and T. Pietrangelo, *Proceedings of the 45th European Microwave Conference* (2015) pp. 666-669.

Finally, a recently introduced approach allows NSMM measurements of biological samples and other liquids by enclosing the samples within molecularly impermeable, chemically inert enclosures. Such enclosures, known as environmental cells, have been used with NSMM [36]. The enclosure is made from an 8 nm to 50 nm thick SiN or $SiO_2$ membrane. The thickness of this wall has to be chosen such that it can sustain the pressure difference between ambient air pressure and the interior. It must also be able to withstand the force due to probe tip contact with the membrane. The imaging depth is on the order of few multiples of probe-membrane radii. Though environmental cells have been used with other techniques such as scanning electron microscopy, the advantage of the microwave technique is that the microwaves represent a low-energy, less-invasive form of penetrating radiation. With the energies in the range of tens of micro-electronvolts, microwave radiation does not affect either electronic states or chemical bonds, thus eliminating destructive effects that may occur in electron, X-ray or optical microscopies.

**References**


[1] S. W. Hell, "Nobel Lecture: Nanoscopy with freely propagating light," *Reviews of Modern Physics* **87** (2015) pp. 1169 – 1181.

[2] W. E. Moerner, "Nobel Lecture: Single-molecule spectroscopy, imaging, and photocontrol: Foundations for super-resolution microscopy," *Reviews of Modern Physics* **87** (2015) pp. 1183-1212.

[3] S. Habuchi, "Super-resolution molecular and functional imaging of nanoscale architectures in life and materials science," *Frontiers in Bioengineering and Biotechnology* **2** (2014) art. no. 20.

[4] D. Axelrod, Cell substrate contacts illuminated by total internal reflection fluorescence," *The Journal of Cell Biology*, **89** (1981) pp. 141-145

[5] E. Betzig, "Nobel Lecture: Single molecules, cells, and super-resolution optics," *Reviews of Modern Physics* **87** (2015) pp. 1153-1167.

[6] E. A. Ash and G. Nicholls, "Super resolution aperture scanning microscope," *Nature* **237** (1972) pp. 510-512.

[7] L. Tetard, A. Passian, K. T. Venmar, R. M. Lynch, B. H. Voy, G. Shekhawat, V. P. Dravid and T. Thundat, "Imaging nanoparticles in cells by nanomechanical holography," *Nature Nanotechnology* **3** (2008) pp. 501-505.

[8] R. Guckenberger, M. heim, G. Cevc, H. F. Knapp, W. Wiegräbe, A. Hillebrand, "Scanning tunneling microscopy of insulators and biological specimens based on lateral conductivity of ultrathin water films," *Science* **266** (1994) pp. 1538-1540.

[9] J. J. Hoh and P. K. Hansma, "Atomic force microscopy for high resolution imaging in cell biology," *Trends in Cell Biology* **2** (1992) pp. 208-213.

[10] Aman Setia and S. Kishore Reddy, "Advancements in microwave breast imaging techniques," *IJREAS* **2** (2012) pp. 1679-1690.

[11] E. C. Burdette, F. L. Cain, and J. Seals, "In vivo Probe Measurement Technique for Determining Dielectric Properties at VHF Through Microwave Frequencies, *IEEE Transactions on Microwave Theory and Techniques* **MTT-28** (1980) pp. 414-427.

[12] T. W. Athe, M. A. Stuchly, and S. S. Stuchly, "Measurement of Radio Frequency Permittivity of Biological Tissues with an Open-Ended Coaxial Line: Part I," *IEEE Transactions on Microwave Theory and Techniques* **MTT-30** (1982) pp. 82-86.

[13] M. A. Stuchly, T. W. Athey, G. M. Samaras, and G. E. Taylor, "Measurement of Radio Frequency Permittivity of Biological Tissues with an Open-Ended Coaxial Line: Part II—Experimental Results," *IEEE Transactions on Microwave Theory and Techniques* **MTT-30** (1982) pp. 87-92.

[14] A. N. Reznik and N. V. Yurasova, “Electrodynamics of near field probing: Application to medical diagnostics,” *Journal of Applied Physics* **98** (2005) art. no. 114701.

[15] E. Alanenyz, T. Lahtinenyx and J. Nuutineny, “Measurement of dielectric properties of subcutaneous fat with open-ended coaxial sensors,” *Phys. Med. Biol.* **43** (1998) pp. 475–485.

[16] X. Wu and O. M. Romahi, “Near-field Scanning Microwave Microscopy for Detection of Subsurface Biological Anomalies,” *Antennas and Propagation Society International Symposium* **3** (2004) pp.2444-2447.

[17] A. Sihvola, *“Electromagnetic mixing formulas and applications”* (The Institution of Engineering and Technology, UK, 1999)

[18] A. N. Reznik and N. V. Yurasova, “Detection of Contrast Objects Inside Biological Media by Near-Field Microwave Diagnostics,” *Technical Physics* **51** (2006) pp. 86–99.

[19] L. A. Klein and C. T. Swift, “An Improved Model for- the Dielectric Constant of Sea Water at Microwave Frequencies,” *IEEE Transactions on Antennas and Propagation* **AP-25** (1977) pp. 104-111.

[20] L. Yang, S. Weerasinghe, P.E. Smith, B. M. Pettitt “ Dielectric response of triplex DNA in ionic solution from simulations” *Biophys J* **69** (1995) pp. 1519–1527.

[21] A. Cuervoa, P. D. Dansb, J. L. Carrascosaa, M. Orozcob, G. Gomilae, and L. Fumagallie, “Direct measurement of the dielectric polarization properties of DNA,” *PNAS* (2014) pp. E3624–E3630.

[22] M. Ch. Biagi, R. Fabregas, G. Gramse, M. Van Der Hofstadt, A. Juárez,F. Kienberger, L. Fumagalli, and G. Gomila, “Nanoscale Electric Permittivity of Single Bacterial Cells at Gigahertz Frequencies by Scanning Microwave Microscopy,” *ACS Nano* **10** (2016) pp.280-288.

[23] G Gramse, M A Edwards, L Fumagalli, and G Gomila, “Theory of amplitude modulated electrostatic force microscopy for dielectric measurements in liquids at MHz frequencies,” *Nanotechnology* **24** (2013) art. no. 415709.

[24] G. Gramse, M. A. Edwards, L. Fumagalli, and G. Gomila, “Dynamic electrostatic force microscopy in liquid media,” *Applied Physics Letters* **101** (2012) art. no. 213108.

[25] G. Gramse, A. Dols-Perez, M. A. Edwards, L. Fumagalli, G. Gomila, “Nanoscale Measurement of the Dielectric Constant of Supported Lipid Bilayers in Aqueous Solutions with Electrostatic Force Microscopy,” Biophysical Journal **104** (2013) pp. 1257-62.

[26] T. X. Wei, X.-D. Xiang, W. G. Wallace-Freedman, P.G. Schultz, “Scanning Tip Microwave Near-Field Microscope” *Applied Physics Letters* **68** (1996) pp. 3506−3508.

[27] M. Tabib-Azar, J. L. Katz, and S. R. LeClair, “Evanescent Microwaves: A Novel Super-Resolution Noncontact Nondestructive Imaging Technique for Biological Applications,” *IEEE Transactions on Instrumentation and Measurement* **48** (1999) pp. 1111-1116.

[28] M. Farina, A. Lucesoli, A. di Donato, D. Mencarelli, L. Maccari, G. Venanzoni, A. Morini and T. Rozzi, "Algorithm for reduction of noise in ultramicroscopy and application to near-field microwave microscopy," *Electronics Letters* **46** (2010) pp. 50-52.

[29] K.J. Coakley, A.Imtiaz, T.M.Wallis, J.C.Weber, S.Berweger, P.Kabos, "Adaptive and robust statistical methods for processing near-field scanning microwave microscopy images," *Ultramicroscopy* **150** (2015) pp. 1-9.

[30] LOCFIT package can be obtained via http://www.locfit.info/

[31] G. Gramse, M. Kasper, L. Fumagalli, G. Gomila, P. Hinterdorfer and F. Kienberger, "Calibrated complex impedance and permittivity measurements with scanning microwave microscopy," Nanotechnology **25** (2014) 145703.

[32] S. Fabiani, A. Lucesoli, A. di Donato, D. Mencarelli, G. Venanzoni, A. Morini,T. Rozzi, and M. Farina, "Dual-Channel Microwave Scanning Probe Microscopy for Nanotechnology and Molecular Biology," *Proceedings of the 40th European Microwave Conference* (2010) pp. 767-770.

[33] M. Farina, D. Mencarelli, A. Di Donato, G. Venanzoni, and A. Morini, " Calibration Protocol for Broadband Near-Field Microwave Microscopy," *IEEE Transactions on Microwave Theory and Techniques* **59** (2011) pp. 2769-2776.

[34] G. P. Kochanski, "Nonlinear alternating-current tunneling microscopy," *Physical Review Letters* **62** (1989) pp. 2285-2288.

[35] M. Farina, A. Di Donato, D. Mencarelli, G. Venanzoni, A. Morini and T. Pietrangelo, "Imaging of biological structures by Near-Field Microwave Microscopy," *Proceedings of the 45th European Microwave Conference* (2015) pp. 666-669.

[36] A. Tselev, J. Velmurugan, A. V. Ievlev, S. V. Kalinin, and A. Kolmakov, "Seeing through Walls at the Nanoscale: Microwave Microscopy of Enclosed Objects and Processes in Liquids," *ACS Nano* **10** (2016) pp. 3562-3570.

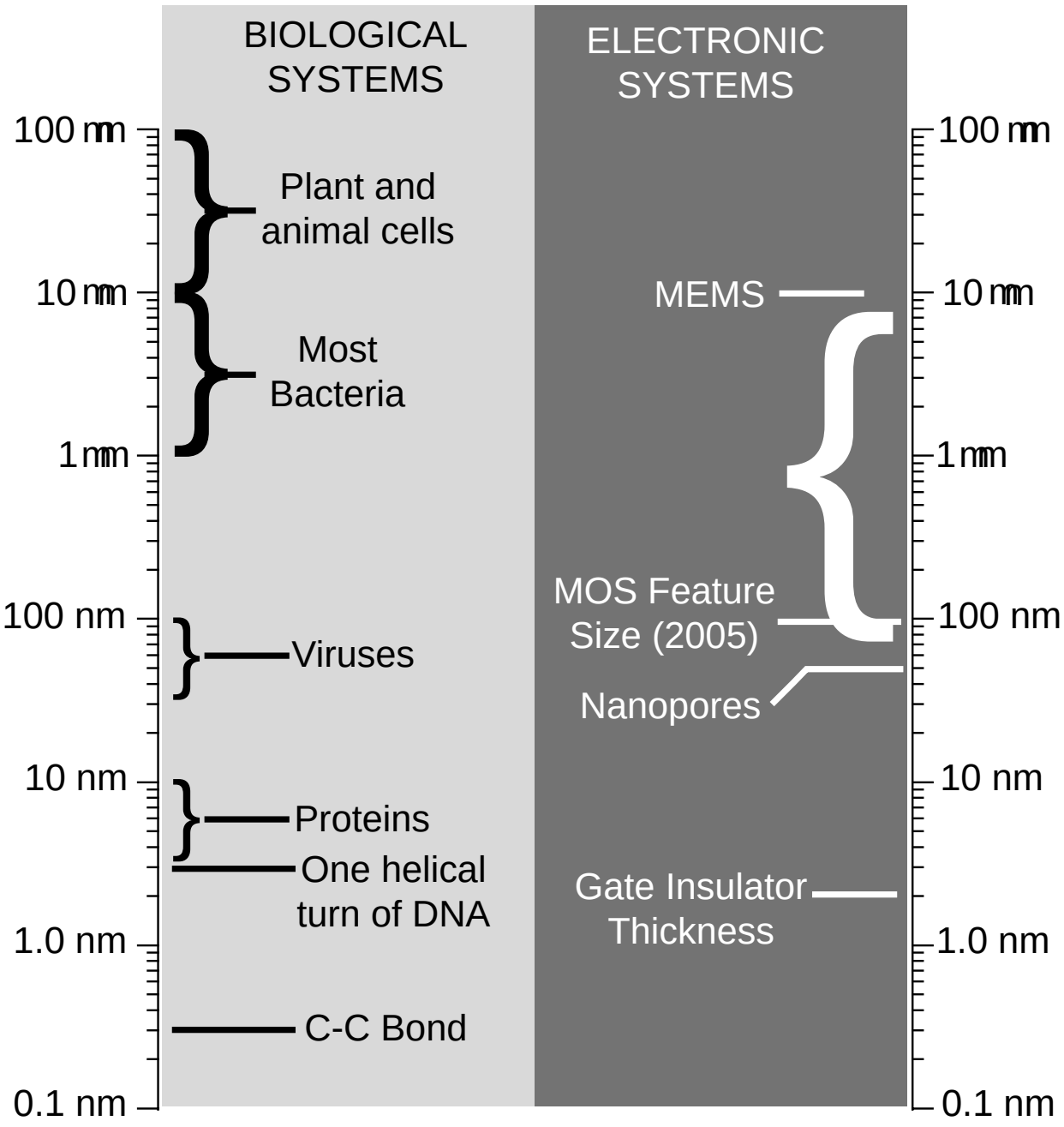
BIOLOGICAL SYSTEMS
ELECTRONIC SYSTEMS
100 mm
10 mm
1 mm
100 nm
10 nm
1.0 nm
0.1 nm
Plant and animal cells
Most Bacteria
Viruses
Proteins
One helical turn of DNA
C-C Bond
MEMS
MOS Feature Size (2005)
Nanopores
Gate Insulator Thickness

FIGURE 14.1

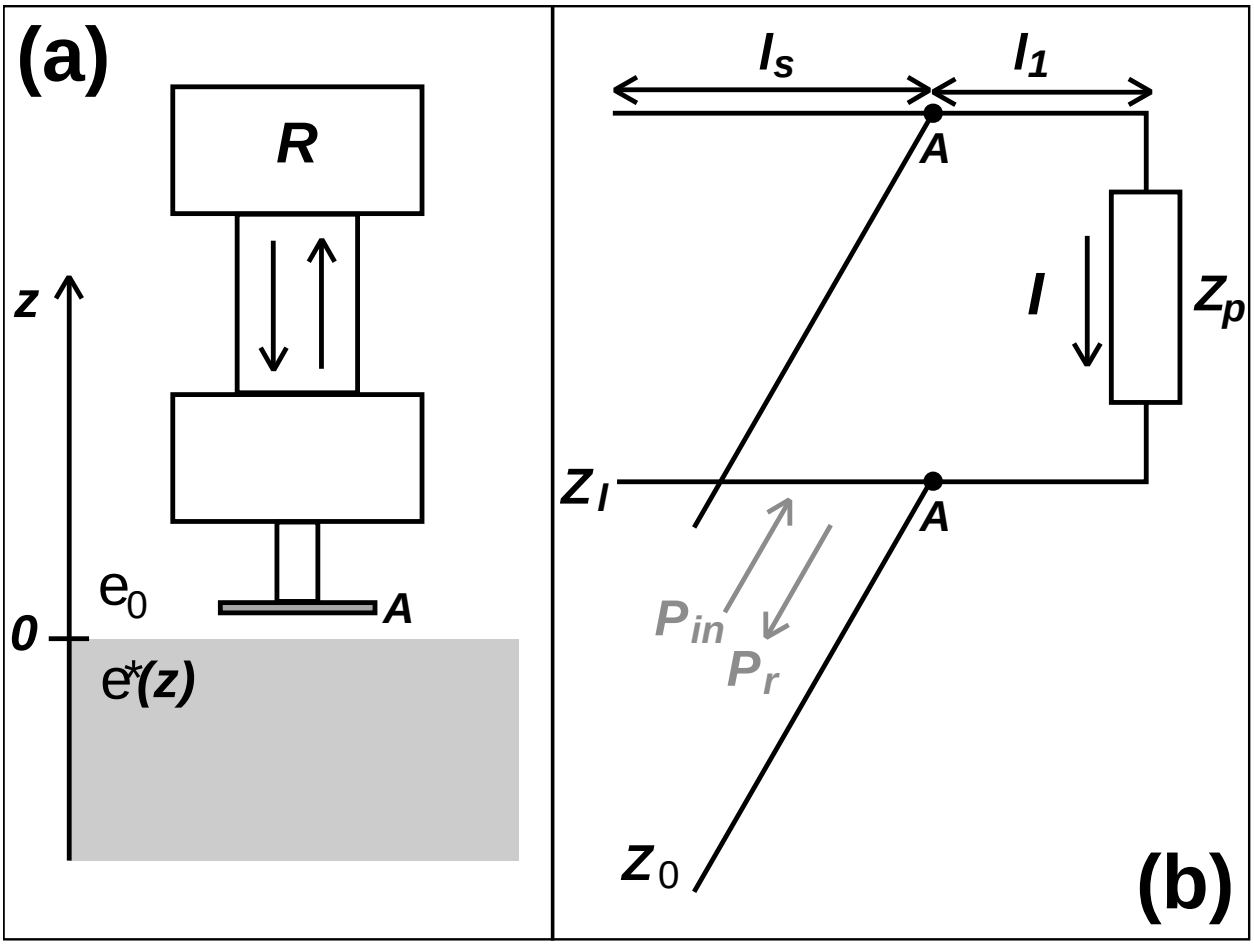


Figure 14.2

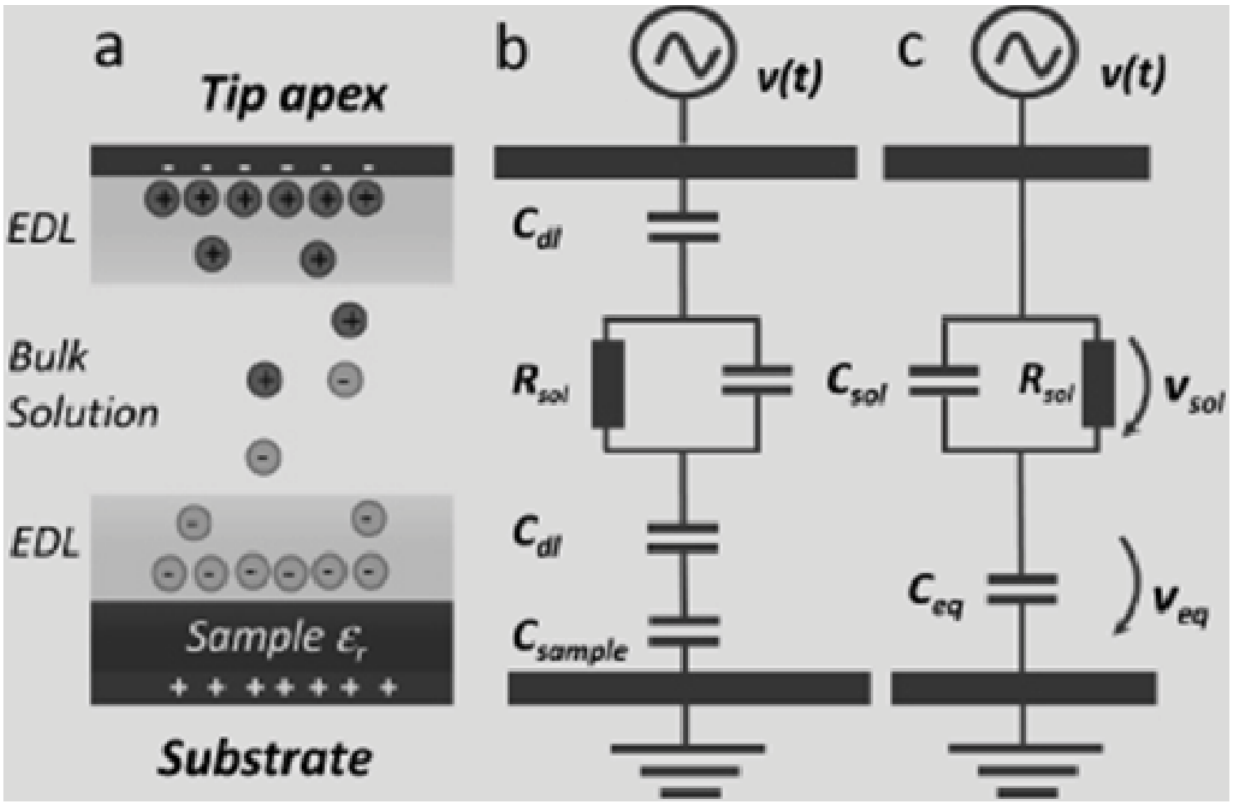
a
Tip apex
EDL
Bulk
Solution
EDL
Sample $\varepsilon_r$
Substrate
b
v(t)
$C_{dl}$
$R_{sol}$
$C_{dl}$
$C_{sample}$
c
v(t)
$C_{sol}$
$R_{sol}$
$v_{sol}$
$C_{eq}$
$v_{eq}$

Figure 14.3

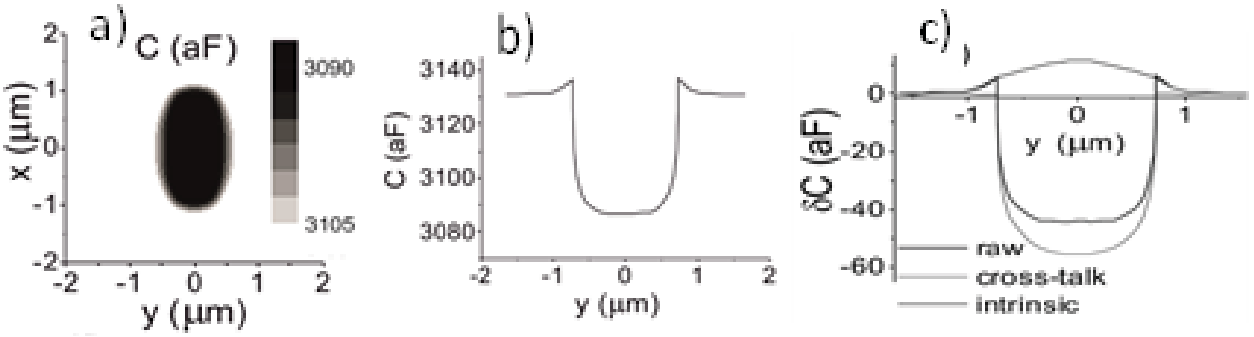
a)
C (aF)
3090
3105
x (µm)
y (µm)
b)
C (aF)
y (µm)
c)
δC (aF)
y (µm)
raw
cross-talk
intrinsic

Figure 144

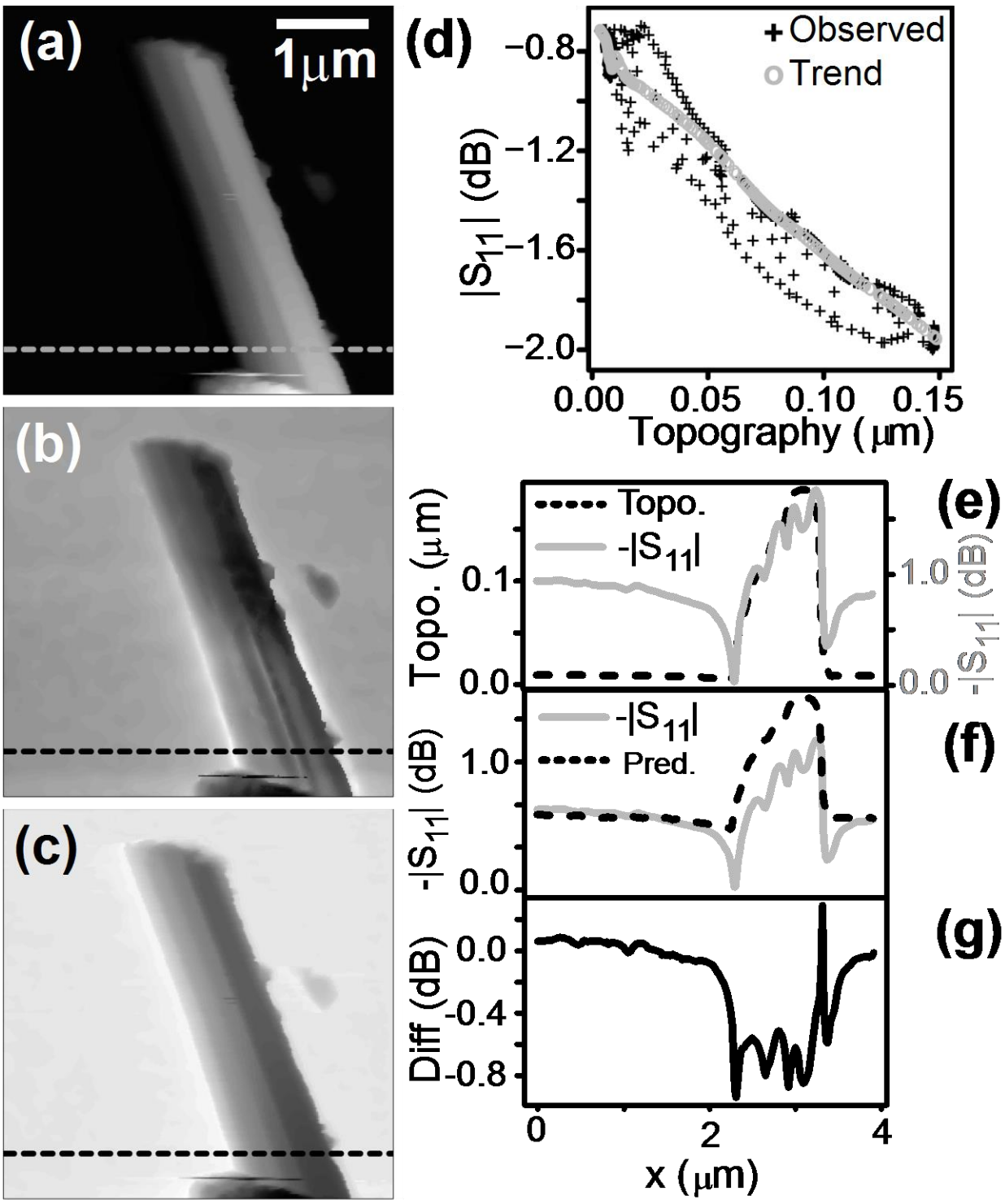
(a)
1μm
(b)
(c)
(d)
Observed
Trend
|S11| (dB)
−0.8
−1.2
−1.6
−2.0
0.00
0.05
0.10
0.15
Topography (μm)
(e)
Topo.
-|S11|
Topo. (μm)
0.1
0.0
1.0
0.0
-|S11| (dB)
(f)
-|S11|
Pred.
-|S11| (dB)
1.0
0.0
(g)
Diff (dB)
0.0
-0.4
-0.8
0
2
4
x (μm)

Figure 14.5

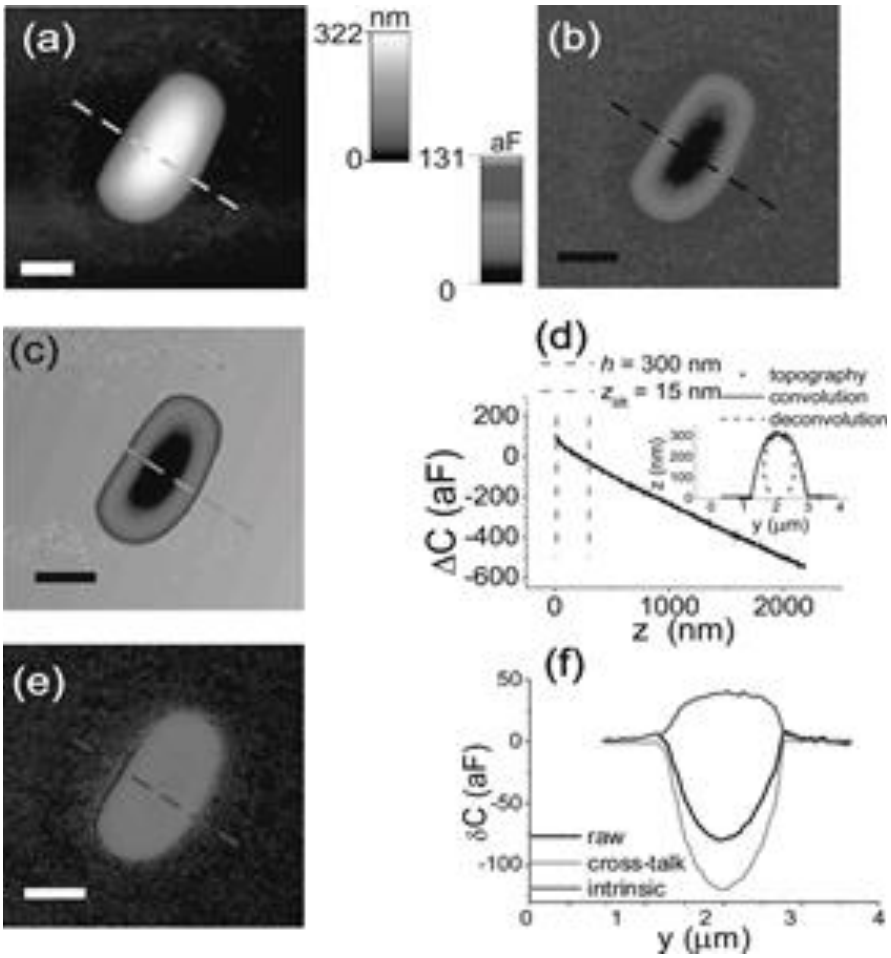
(a)
322
nm
0
131
aF
0
(b)
(c)
(d)
h = 300 nm
z_tip = 15 nm
topography
convolution
deconvolution
200
0
-200
-400
-600
ΔC (aF)
0
1000
2000
z (nm)
z (nm)
y (μm)
(e)
(f)
50
0
-50
-100
δC (aF)
raw
cross-talk
intrinsic
0
1
2
3
4
y (μm)

Figure 146

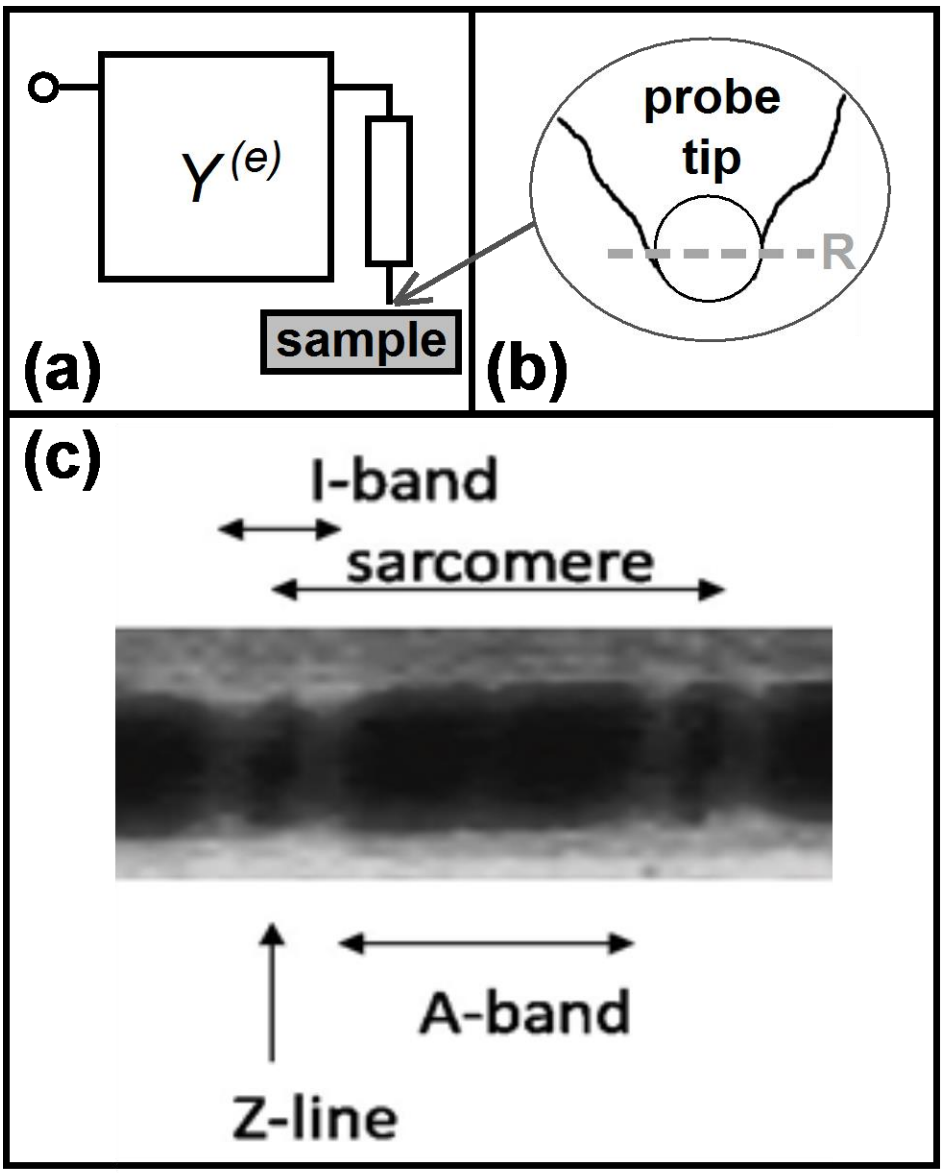


**Figure 14.7**